Black hole echology: The observer's manual

Qingwen Wang[*] and Niayesh Afshordi[†]

*Perimeter Institute for Theoretical Physics, 31 Caroline Street North, Waterloo, Ontario N2L 2Y5, Canada
and Department of Physics and Astronomy, University of Waterloo, 200 University Avenue West,
Waterloo, Ontario N2L 3G1, Canada*

While recent detections of gravitational waves from the mergers of binary black holes match well with the predictions of General Relativity, they cannot directly confirm the existence of event horizons. Exotic compact objects are motivated by quantum models of black holes and can have exotic structure (or a "wall") just outside the (would-be) horizon. Exotic compact objects produce ringdown waveforms similar to the General Relativistic black holes, but they are followed by delayed "echoes." By solving linearized Einstein equations, we can model these echoes and provide analytic templates that can be used to compare to observations. For concreteness, we consider the GW150914 event, detected by the LIGO/Virgo Collaboration, and study the model dependence of its echo properties. We find that echoes are reasonably approximated by complex Gaussians, with amplitudes that decay as a power law in time, while their width in time (frequency) grows (shrinks) over subsequent echoes. We also show that trapped modes between a perfectly reflecting wall and angular momentum barrier in the Kerr metric can exhibit superradiant instability over long times, as expected.

I. INTRODUCTION

Motivated by the black hole (BH) information paradox and cosmological constant problems, it has been suggested that nonperturbative quantum gravitational effects may lead to Planck-scale modifications of BH horizons. Proposals to solve the BH information paradox [67] include gravastars [1], fuzzballs [2–6], and firewalls [7,8], among others [9,10]. These exotic compact objects (ECOs) all modify the standard structure of BH horizons and should form by Page time $\sim M^3$ but can emerge as early as the "scrambling time" $\sim M \log M$ [11,12].

Gravitational aether theory [13,14], which modifies the Einstein field equations by adding an incompressible fluid (aether), is a possible solution to the cosmological constant problem(s). BH solutions in this theory link the BH mass with the aether pressure at infinity and yield a pressure comparable to the observed dark energy pressure for stellar BH masses of 10–100 $M_\odot$. The solution of the modified Einstein field equation deviates from General Relativity (GR) within the order of the Planck length proper distance outside the (would-be) horizon. It is also suggested that replacing the horizon with a "wall" could be a source of high energy astrophysical neutrino flux [15], which is a possible source for the PeV neutrinos recently detected by the IceCube observatory.

A concrete physical model for replacing the event horizon due to quantum gravitational effects is provided in Ref. [16]. The spacetime ends at about the order of the Planck length proper distance outside the (would-be) horizon with a wall containing a surface fluid. It is then shown that Israel junction conditions imply that the fluid has the thermodynamic entropy matching the Bekenstein-Hawking area law, for charged rotating BHs (also see Ref. [17] for a similar horizonless spacetime solution).

Recent detections of gravitational waves from binary BH mergers by the LIGO/Virgo Collaboration [18–26] provide a way to test the structure around the horizon scale. Shortly after LIGO's first detection, GW150914, Refs. [27,28] argued that introducing a wall to replace horizon might yield a ringdown waveform similar to GR BHs but produce delayed echoes (see Refs. [29,30] for a review) in the gravitational wave signal. Using a phenomenological template by truncating the GR merger waveforms, Ref. [31] carried out the first search for echoes and claimed a 2.5σ tentative evidence for them in the first three (candidate) events in the LIGO public data (but see Refs. [32–34] for a critique/rebuttal).

An independent search [35], using a different methodology, has recently found evidence for echoes in each of LIGO's merger events (with the notable exception of GW150914) at $\sim 3\sigma$ significance level. However, we should note that the echoes reported in Refs. [31,35] are for different events, even though they are both broadly consistent with the hypothesis of near-horizon Planck-scale

[*]qwang@pitp.ca
[†]nafshordi@pitp.ca

structure. In particular, Refs. [33,34] failed to find echoes in GW151226, which has the most significant evidence for echoes in Ref. [35], suggesting that the two methods capture different parts of the echo waveform.

Most recently, Ref. [36] claimed a tentative detection of (lower harmonics of) echoes, at 4.2σ level, from a "black hole" remnant in the aftermath GW170817 binary neutron star merger.

While one may consider other phenomenological echo templates (e.g., Ref. [37]), more realistic templates for fitting data may be found by solving (linearized) Einstein equations with modified boundary conditions near the horizon. Along this direction, most studies have so far focused on Schwarzschild BHs (e.g., Refs. [27,28,38–41]). In this paper, we extend this to the Kerr metric as realistic BHs have spin. Reference [42] also presented echo templates by modeling the reflectivity of the angular momentum barrier in the Kerr spacetime. We, however, model the propagation in the full spacetime, which provides a more realistic treatment at lower frequencies.

Another related work is Ref. [43], which studies the echoes of scalar Gaussian wave packets in Kerr-like wormholes. In contrast, we study generic propagation in Kerr spacetime, with arbitrary boundary conditions, which can be applied not only to scalar fields ($s = 0$) but also massless Dirac ($s = \pm 1/2$), electromagnetic ($s = \pm 1$), or gravitational ($s = \pm 2$) fields. Interestingly (but not surprisingly), we come to some similar conclusions, e.g., (i) spinning ECOs give rise to unstable modes which, however, do not affect the echoes till very late times (depending on whether the initial frequency range is within the superradiance regime), and (ii) it is hard to make a model-independent prediction for the first echo.

A related phenomenological issue that arises when we replace the horizon with a wall is the emergence of superradiant instability for horizonless ergoregions [44–47]. While this might suggest the long-term instability of spinning ECOs, which may be in conflict with astrophysical spin measurements for BHs [48], it was suggested by Ref. [49] that an absorption rate of the wall as small as 0.4% is sufficient to quench the instability completely.

We organize this paper as follows. Section II provides the linear Einstein equations and boundary conditions used. Instead of the normal boundary condition with no outgoing wave on the horizon, we put a wall standing just outside the would-be horizon. The reflection rate of the wall depends on the specific model of quantum BHs. Section III presents echo solutions for different positions of a perfect wall and time delays of a geometric formula given in Ref. [31], while Sec. IV discusses how the superradiance of Kerr geometry is manifested in echo templates. In Sec. V, we provide an analytic fit to the echo templates, based on solutions in Sec. III. We explore a soft wall with frequency-dependent reflection as well as nonlinear corrections to initial conditions in Sec. VI for a more realistic picture. In the

Appendix, we briefly discuss ergoregion instability developed in the presence of a perfect wall. While in principle the instability is significant at high spins, we show that these instabilities do not affect the first several echoes of typical binary merger events. Finally, Sec. VII concludes our work.

If not specified, we use units with $G = \hbar = k_B = c = 1$. For concreteness, we use the best-fit properties and waveforms resulting from the GW150914 merger event, provided by the LIGO/Virgo Collaboration [18,19] [50]. In particular, the detector frame mass and reduced spin parameter of the remnant used for the echo calculation are $M_{\text{fin}} = 67.6 M_\odot$ and $a = 0.67$. Echo templates for other final masses can be found by rescaling our analytic templates, as long as the dimensionless binary properties are not too different from those of GW150914.

II. PROPAGATION AND BOUNDARY CONDITIONS IN KERR SPACETIME

We study the propagation of gravitational waves using linearized Einstein equations in Kerr geometry which describes the spacetime of a spinning BH. In order to model an ECO, we simply replace the Kerr event horizon with a wall, where boundary conditions for linear perturbations are modified. The initial condition here is an incoming wave packet h_{in} from infinity, and we calculate the outgoing wave packet h_{out} by solving the linear Einstein equations. As usual, we use the Newman-Penrose (NP) formalism which greatly simplifies perturbation in the Kerr metric, reducing to only a single master equation (known as the Teukolsky equation) which describes propagation of all scalar ($s = 0$), massless Dirac ($s = \pm 1/2$), electromagnetic ($s = \pm 1$), and gravitational ($s = \pm 2$) fields (see Ref. [51] for details),

$$\left[\frac{(r^2 + a^2)^2}{\Delta} - a^2\sin^2\theta\right]\frac{\partial^2\psi}{\partial t^2} + \frac{4Mar}{\Delta}\frac{\partial^2\psi}{\partial t\partial\varphi}$$
$$+ \left(\frac{a^2}{\Delta} - \frac{1}{\sin^2\theta}\right)\frac{\partial^2\psi}{\partial\varphi^2} - \Delta^{-s}\frac{\partial}{\partial r}\left(\Delta^{s+1}\frac{\partial\psi}{\partial r}\right)$$
$$- \frac{1}{\sin\theta}\frac{\partial}{\partial\theta}\left(\sin\theta\frac{\partial\psi}{\partial\theta}\right) - 2s\left[\frac{a(r - M)}{\Delta} + \frac{i\cos\theta}{\sin^2\theta}\right]\frac{\partial\psi}{\partial\varphi}$$
$$- 2s\left[\frac{M(r^2 - a^2)}{\Delta} - r - ia\cos\theta\right]\frac{\partial\psi}{\partial t}$$
$$+ (s^2\cos^2\theta - s)\psi = 0, \tag{1}$$

where the field ψ for each spin weight s corresponds to NP quantities presented in Table I.

TABLE I. Corresponding field ψ for different spin weight s in Master equation. Here, $\rho^{-1} = -(r - ia\cos\theta)$.

s	0	$-1/2, 1/2$	$-1, 1$	$-2, 2$
ψ	Φ	$\chi_0, \rho^{-1}\chi_1$	$\phi_0, \rho^{-2}\phi_2$	$\Psi_0, \rho^{-4}\Psi_4$

The Teukolsky equation (1) is separable in coordinates in the frequency domain and can be decomposed into four ODEs. Furthermore, the symmetries in time and azimuth allow for Fourier space decomposition in t and φ,

$$\psi = \frac{1}{2\pi} \int d\omega e^{i(-\omega t + m\varphi)} S[\theta] R[r], \qquad (2)$$

$$\Delta^{-s} \frac{d}{dr} \left(\Delta^{s+1} \frac{dR}{dr} \right)$$
$$+ \left[\frac{K^2 - 2is(r-M)K}{\Delta} + 4is\omega r - \lambda \right] R = 0, \quad (3)$$

$$\frac{1}{\sin\theta} \frac{d}{d\theta} \left(\sin \frac{dS}{d\theta} \right) + \left(a^2\omega^2\cos^2\theta - \frac{m^2}{\sin^2\theta} - 2a\omega s \cos\theta \right.$$
$$\left. - \frac{2ms\cos\theta}{\sin^2\theta} - s^2\cot^2\theta + s + A_{slm} \right) S = 0, \qquad (4)$$

where $K = (r^2 + a^2)\omega - am$ and $\lambda = A_{slm} + a^2\omega^2 - 2am\omega$. The solution for the angular mode is a spin-weighted spheroidal harmonic (the full discussion can be found in Ref. [52]). We solve the radial mode numerically based on Brito *et al.* [53], with the publicly available *Mathematica* code, which was developed to study superradiance in the Kerr metric [54]. Equation (3) has the following asymptotic solutions,

$$R = \mathcal{T}\Delta^{-s}e^{-ik_h r^*} + \mathcal{O}e^{ik_h r^*}, \quad r \to r_+, \qquad (5)$$

$$R = \mathcal{I}\frac{e^{-i\omega r^*}}{r} + \mathcal{R}\frac{e^{i\omega r^*}}{r^{2s+1}}, \quad r \to \infty, \qquad (6)$$

where r^* is the tortoise coordinate (defined as $r^* = \int \frac{r^2+a^2}{r^2-2Mr+a^2} dr$ that approaches $-\infty$ at horizon), $k_h = \omega - \frac{am}{2Mr_+}$, and $r_+ = M + \sqrt{M^2 - a^2}$.

In classical General Relativity, everything that reaches the horizon will fall into the BH, and thus there is no outgoing wave at $r \to r_+$, i.e., $\mathcal{O} = 0$. However, for ECOs, we assume that quantum gravity effects replace the horizon with a (partially) reflective wall standing the order of Planck length proper distance outside the (would-be) horizon. We shall assume that this modifies the boundary condition so that the wall reflects the incoming energy flux (see Ref. [42] for the definition of energy near horizon) with a rate R but does not change the phase:

$$|\mathcal{O}|^2 = R_{wall} \left| \frac{C}{D} \right|^{s/2} |\mathcal{T}|^2,$$

$$\arg[\mathcal{T}\Delta^{-s}e^{-ik_h r^*}] = \arg[\mathcal{O}e^{ik_h r^*}] \quad \text{when } r \to r_{wall}, \qquad (7)$$

$$C = B\{-36a^2\omega^2 + 36am\omega + [\lambda + (s+1)s - 2]^2\}$$
$$+ \{2[\lambda + (s+1)s] - 1\}(96a^2\omega^2 - 48am\omega)$$
$$+ 144\omega^2(M^2 - a^2), \qquad (8)$$

$$B = [\lambda + s(s+1)]^2 + 4ma\omega - 4a^2\omega^2,$$

$$D = 256k_h^2(2Mr_+)^8 \left[k_h^2 + \frac{4(M^2-a^2)}{(4Mr_+)^2} \right]^2$$
$$\times \left[k_h^2 + \frac{16(M^2-a^2)}{(4Mr_+)^2} \right]. \qquad (9)$$

$R_{wall} = 1$ would correspond to a perfectly reflective wall, but the actual reflectivity and phase change depend on the specific quantum gravity model for ECOs. In the rest of the paper, we will present solutions to these equations with different choices of the reflectivity and discuss the important properties of solutions, such as echo templates, time delays, and superradiant instability.

III. MAKING ECHOES

Realistic predictions for echo waveforms requires nonlinear simulations of the mergers of binary ECOs in full general relativity. As a consistent covariant formulation for dynamics of ECOs is yet nonexistent, we have to rely on approximate methods to produce realistic echo templates. In order to do this using linear theory, we instead custom design an ingoing wave packet $\hat{h}_{in}$ at infinity so that the outgoing waveform matches the LIGO best-fit template $\hat{h}_{LIGO}$ (without a wall). The higher frequencies will go across the barrier and fall into the BH, as shown in Fig 1 (left), while the lower frequencies are reflected. We thus assume

$$\hat{h}_{LIGO}(\omega) = R_{BH}(\omega)\hat{h}_{in}(\omega), \qquad (10)$$

where $R_{BH}(\omega)$ is the reflectivity of the Kerr angular momentum barrier. For an ECO, however, we have one more barrier near the would-be horizon as shown in Fig 1 (right). Wave packets with intermediate frequencies can now be trapped between two barriers and leak slowly every time when they hit the angular momentum barrier. Therefore, ECOs would have a similar ringdown waveform as classical BHs, but they are followed by delayed slowly decaying echoes.

$$\hat{h}_{out}(\omega) = R_{ECO}(\omega)\hat{h}_{in}(\omega) = R_{ECO}(\omega)\frac{\hat{h}_{LIGO}(\omega)}{R_{BH}(\omega)}f_{cutoff}(\omega),$$
$$\qquad (11)$$

where $f_{cutoff}(\omega)$ is a low-pass filter introduced to suppress numerical noise at high frequencies, as the reflectivity of the
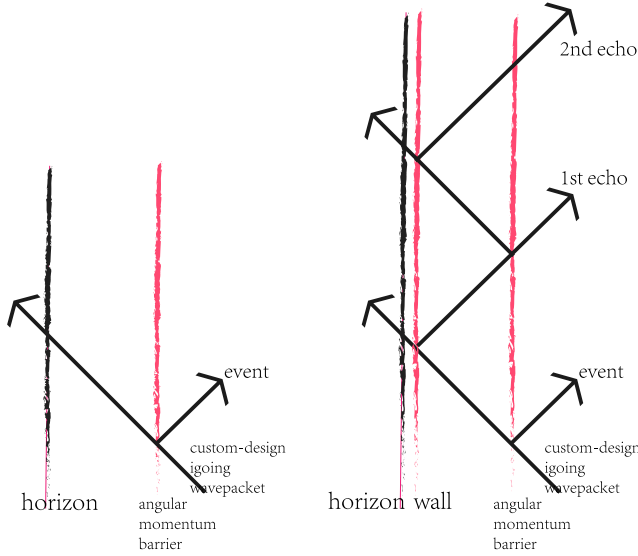
FIG. 1.   BHs and ECOs with an ingoing wave packet. For BHs, the angular momentum barrier reflects the low frequency modes, but higher frequencies cross the barrier and fall through the horizon. For ECOs with a wall standing the order of Planck length proper distance outside the (would-be) horizon, modes with intermediate frequencies can be trapped between the wall and the angular momentum barrier, slowly leaking out as repeating echoes.

Kerr angular momentum barrier $R_{\mathrm{BH}}(\omega)$, in the denominator, vanishes at high frequencies. Luckily, high frequencies leak out quickly in the first echo and have a small effect on the subsequent echoes. Our choice of f_{cutoff} does not affect the second and later echoes, but it changes the first echo slightly by cutting the high frequency noise,

$$\hat{h}_{\mathrm{out,fin}} = \hat{h}_{\mathrm{out}} f_{\mathrm{cutoff}}, \qquad (12)$$

$$f_{\mathrm{cutoff}} = \exp\left[-\frac{1}{2}\left(\frac{2\pi f(\mathrm{Hz}) - 299.495}{1347.73}\right)^{16}\right], \quad (13)$$

where $\omega = 2\pi f$.

With the equations and boundary conditions given in the last section, we can numerically solve for R_{BH} and R_{ECO} as a function of frequency. We use LIGO event GW150914 with $a = 0.67$, $M = 62 M_{\odot}$, and $z = 0.09$. The mass is measured in the source frame, and the finial mass used in our calculation is the mass in the detector frame $M_{\mathrm{fin}} = (1 + z)M$. The waveform is dominated by the $(l, m) = (2, 2)$ mode, which we shall focus on for the rest of the paper [55].

The time dependence of the waveform can then be obtained by Fourier transforming $\hat{h}_{\mathrm{out}}(\omega)$ and is shown in Fig. 2. We see that changing the position of the wall changes the time delay between the echoes but does not affect the individual echo waveforms significantly (as long as the wall is close the would-be horizon). As we see in Fig. 1, in the geometric optics approximation, the time delay between echoes, $\Delta t_{\mathrm{echo,geom}}$, is given by the travel time from the angular momentum barrier to the wall and back [31]:

$$\Delta t_{\mathrm{echo,geom}} = 2r_* |_{r_{\mathrm{wall}}}^{r_{\mathrm{barrier}}} = 2\int_{r_{\mathrm{wall}}}^{r_{\mathrm{barrier}}} dr \frac{r^2 + a^2 M^2}{r^2 - 2Mr + a^2 M^2}$$

$$= 2r_{\mathrm{barrier}} - 2r_{\mathrm{wall}} + 2\frac{r_+^2 + a^2 M^2}{r_+ - r_-} \ln\frac{r_{\mathrm{barrier}} - r_+}{r_{\mathrm{wall}} - r_+}$$

$$- 2\frac{r_-^2 + a^2 M^2}{r_+ - r_-} \ln\frac{r_{\mathrm{barrier}} - r_+}{r_{\mathrm{wall}} - r_-}. \qquad (14)$$

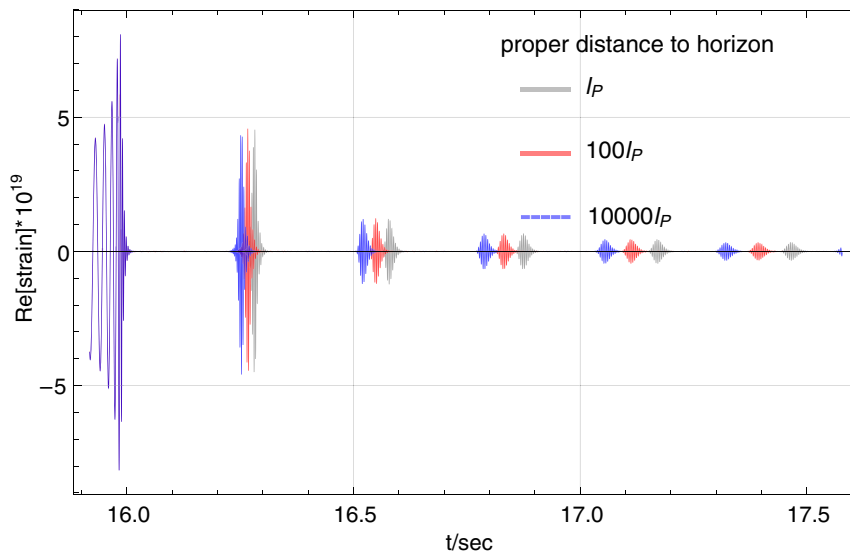This can be well approximated by the following fitting function,

FIG. 2.   Echoes with different wall positions. Changing the positions of wall does not influence the shape of echoes a lot, but when putting wall closer to the would-be horizon and away from angular momentum barrier, the time delay becomes bigger.
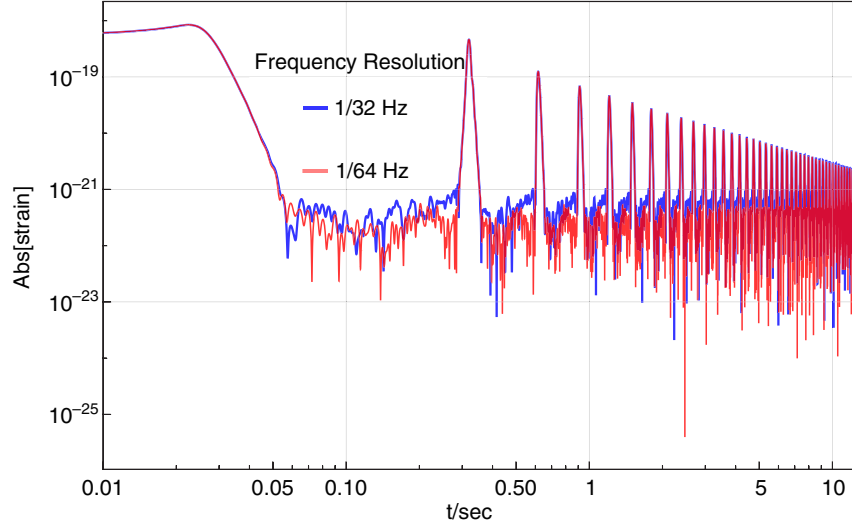
FIG. 3.   Predicted echoes for LIGO event GW150914 in the time domain with different resolution, assuming a prefect wall at a Planck length proper distance outside the horizon.

$$\Delta t_{\text{echo,geom}} = 2\frac{r_+^2 + a^2 M^2}{r_+ - r_-}\ln\frac{M}{r_{\text{wall}} - r_+} + MG(a), \quad (15)$$

$$G(a) \simeq \frac{0.335}{a^2 - 1} + 4.77 + 7.42(a^2 - 1) + 4.69(a^2 - 1)^2, \quad (16)$$

$$r_{\text{wall}} - r_+ = \frac{\sqrt{1 - a^2}\, d_{\text{wall}}^2}{4M(1 + \sqrt{1 - a^2})}, \quad (17)$$

where we find the fit of $G(a)$ for the angular momentum barrier of $l = m = 2$ mode, while d_{wall} is the proper distance from the wall to the would-be horizon. The latter is expected to be comparable to Planck length for ECOs of quantum gravitational nature, but Δt_{echo} only depends on the exact value of d_{wall} logarithmically (see Fig. 2).
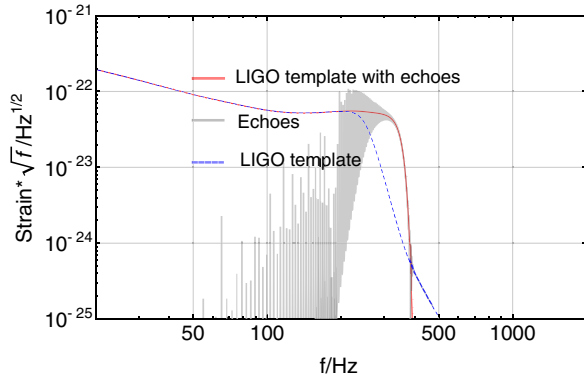

FIG. 4.   Predicted echoes for LIGO event GW150914 in the frequency domains, assuming a prefect wall at a Planck length proper distance outside the horizon.

The echoes in both the time and frequency domains for the LIGO event GW150914 are shown in Figs. 3 and 4 with a perfect wall standing a Planck length proper distance outside the (would-be) horizon. Here, we show the amplitude spectral density, which is the square root of the power spectral density. The latter is the average of the square of the fast Fourier transforms of the model. In the next section, we will study the structure of the echo in the frequency domain and present how superradiance affects the structure of the echo.

IV. SUPERRADIANCE

Scattering off the Kerr BH can lead to superradiance of modes with frequency $0 < \omega < m\Omega_{\text{H}}$, which can extract energy from a spinning background [56]. Adding a (partially) reflective wall near the horizon could turn this amplification to an instability, since modes trapped between the wall and the angular momentum barrier can extract the spin energy repeatedly [44,45]. In this section, we study this effect for the echoes in frequency domains.

There is an odd-looking spike in Fig. 4's frequency domain around 183 Hz (see the top panel in Fig. 5 for a zoom-in). Indeed, this is exactly the threshold frequency for the superradiance. This is demonstrated in the middle panel of Fig. 5, which shows the scattering amplification with the horizon, perfect wall, and soft wall around that frequency. The vertical axis is the relative energy, extracted from around black hole by scattered gravitational waves. The blue dashed line shows superradiance slowly turning off with increasing the frequency, and we confirm that it ends exactly at frequency $f_{\text{max}} = am/[2\pi(r_+^2 + a^2)] = 183$ Hz, for $m = 2$ as shown in the plot. In contrast, superradiance by the soft wall (gray and thin curve) occurs at resonance peaks, corresponding to the ergoregion trapped mode
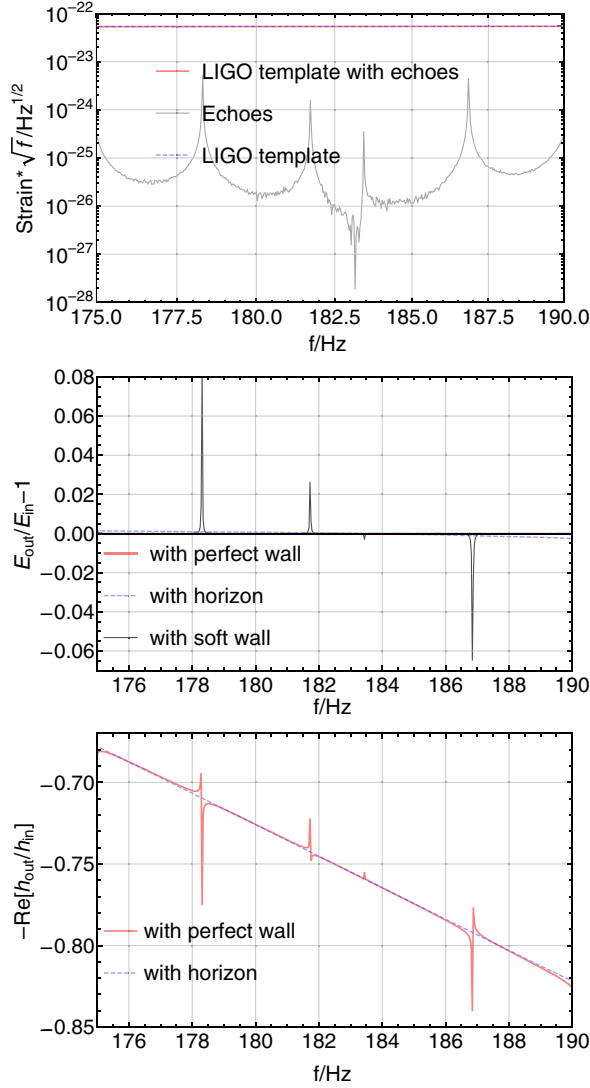
FIG. 5. Superradiance in the frequency domain for a GR Kerr BH and ECO with a wall.

(for more details, see the Appendix). Since superradiance ends at 183 Hz, the resonance peaks shift the direction, which is the reason we have an odd spike in Figs. 4's and 5's top panels.

The perfect wall (the red thick curve) in Fig. 5's middle panel is a constant zero without any resonance peaks, since a perfect reflective wall kills superradiance, as all the energy that goes in comes out eventually (see the Appendix for a subtlety in this argument). However, the odd spike structure remain in the amplitudes, as shown in Fig. 5's bottom panel, where we change the vertical axis to a real part of an outgoing to ingoing wave at infinity. We still see the sign flip in the resonance structure at 183 Hz.

In the next section, we study the echo templates resulting from solving the linearized Einstein equations, which improves the simplistic geometric picture in Fig. 1.

V. MINIMAL ECHO TEMPLATES

Now that we have numerical predictions for echoes, we would like to provide simple fitting functions that could be used for quick visualization and data-fitting purposes. We call these fitting functions templates. In order to find our templates, we define echoes in the time domain by the regions that surround the peaks of $|h(t)|$ and exceed a limit: $\ln\left[|h(t)|/|h|_{\mathrm{max,n}}\right] > -1, -1.5$ or -2. $|h|_{\mathrm{max,n}}$ is the height of the nth peak of $|h(t)|$, which we call the nth echo. Then, we fit the nth echo to a complex Gaussian,

$$h_n(t) = \exp[\Psi_n(t) + I\Phi_n(t)], \tag{18}$$

$$\Psi_n(t) = a_0 + a_1 t + a_2 t^2, \tag{19}$$

$$\Phi_n(t) = b_0 + b_1 t, \tag{20}$$

where a_0, a_1, a_2, b_0, and b_1 are real numbers. This form is the same as fitting the nth echo to $A\exp\left[\frac{(t-t_0)^2}{2\sigma^2}\right]$, where A and t_0 are complex, while the width σ is real.

As an example, Fig. 6 compares the numerical solutions and Gaussian fits for the 2nd, 10th, and 30th echoes, with the time origin shifted to the center of each echo and fitting the region with $\ln\left[|h(t)|/|h|_{\mathrm{max,n}}\right] > -1.5$.

Within this approximation, there are five real parameters for every echo that quantify its amplitude, width, and center, in both the time and frequency domains, as well as the overall phase at the center of the echo, as shown in Table II.
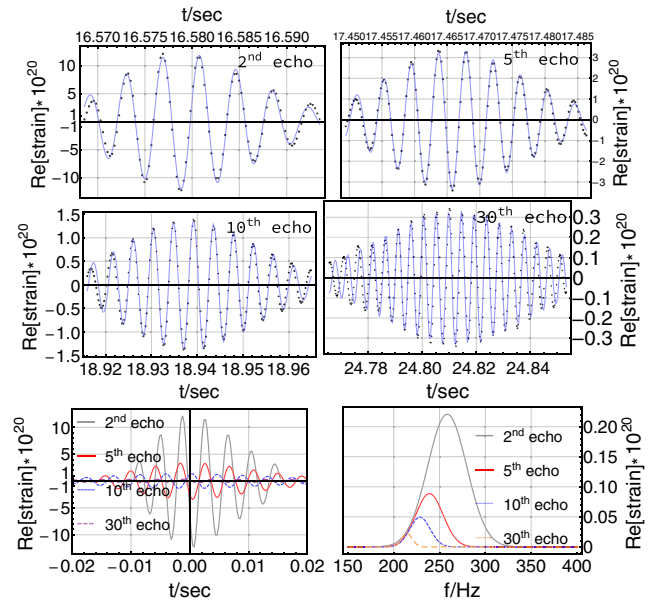

FIG. 6. Best-fit Gaussians to the 2nd, 5th, 10th, and 30th echoes within $\ln\left[|h(t)|/|h|_{\mathrm{max,n}}\right] > -1.5$. We see that, as high frequency modes leak out faster, later echoes decay in amplitude and become wider in the time domain, and high frequency is cut in the frequency domain.

TABLE II.   Some physical quantities of a single echo defined by the five parameters from the Gaussian echo template [Eq. (19)].

	Width	Center	Peak amplitude
Time	$\sqrt{-1/(2a_2)}$	$-a_1/2a_2$	$\exp[a_0 - a_1^2/4a_2]$
Frequency	$\sqrt{-2a_2}/(2\pi)$	$b_1/(2\pi)$	$\exp[a_0 - a_1^2/4a_2 - 1/2\log[2\sqrt{a_2^2}]]$
Overall phase	$b_0 - b_1 a_1/(2a_2)$		

TABLE III.   Best-fit Gaussian echo template quantities (see Table II and Fig. 7), for our minimal model of GW150914.

Peak amplitude in time (strain)	$2.91 \times 10^{-19}/n^{1.32}$
Width in time (msec)	$4.29 + 0.883n$
Correction to $\Delta t_{\text{echo,geom}}$ (msec)	$1.52 + 1.71/(1+n)$
Peak frequency (Hz)	$177 + 102/n^{0.3}$
Overall phase	$-7.26 + 27.1n^{0.945} + 22.6n$

Table III provides the best-fit parameters of our echo templates for all echoes, based on the LIGO event GW150914 and averaging over the best-fit functions with different echo domains $\ln[|h(t)|/|h|_{\text{max,n}}] > -1, -1.5$, or -2.

The best fits for each echo domain are also provided in Fig. 7. For correction to $\Delta t_{\text{echo,geom}}$, we define the time delay as $\Delta t_n = t_n - t_{n-1}$. For all other plots, the first echo is not included since it is very sensitive to the properties of the wall as well as nonlinear effects from the early stage of merger (see details in Sec. V). The top three panels in Fig. 7 show the time domain properties as a function of the echo number. Starting from the left, peak echo amplitudes in time are all fit well by decaying power laws (Ref. [57]

argues that the decay of echoes at early stages is polynomial). In the middle is the width of the echoes, becoming wider for later echoes in the time domains, as the high frequency modes leak out more quickly. The top right panel gives a correction to $\Delta t_{\text{echo,geom}}$ (15), while the bottom left panel shows the decay of the mean echo frequency. The bottom middle and right provide the overall phase at t_{center} and the residuals of the best fit for the phase. We only show the residuals for the phase, as the numerical error for the phase is relatively big.

To visualize the quality of the template to fit data, Fig. 8 shows the $\text{SNR}_{\text{temp}}/\text{SNR}_{\text{model}}$, where $\text{SNR}_{\text{model}}$ is the predicted signal-to-noise ratio for our numerical solution of echoes (assuming white noise) while SNR_{temp} is a reduced value, if we use our Gaussian approximations of Fig. 6 (gray circles in Fig. 8). Using a second fit for how properties (i.e., width, center, and amplitude) of $\Psi_n(t) = \log|h_n(t)|$ depend on n (Table III) further reduces SNR_{temp} (red triangles in Fig. 8). We notice that the quality of Gaussian fit drops for later echoes, which could be due to either the build-up of numerical error or systematic deviations from a single Gaussian fit. The secondary fit for Ψ_n vs n further reduces the SNR as the width in time and time
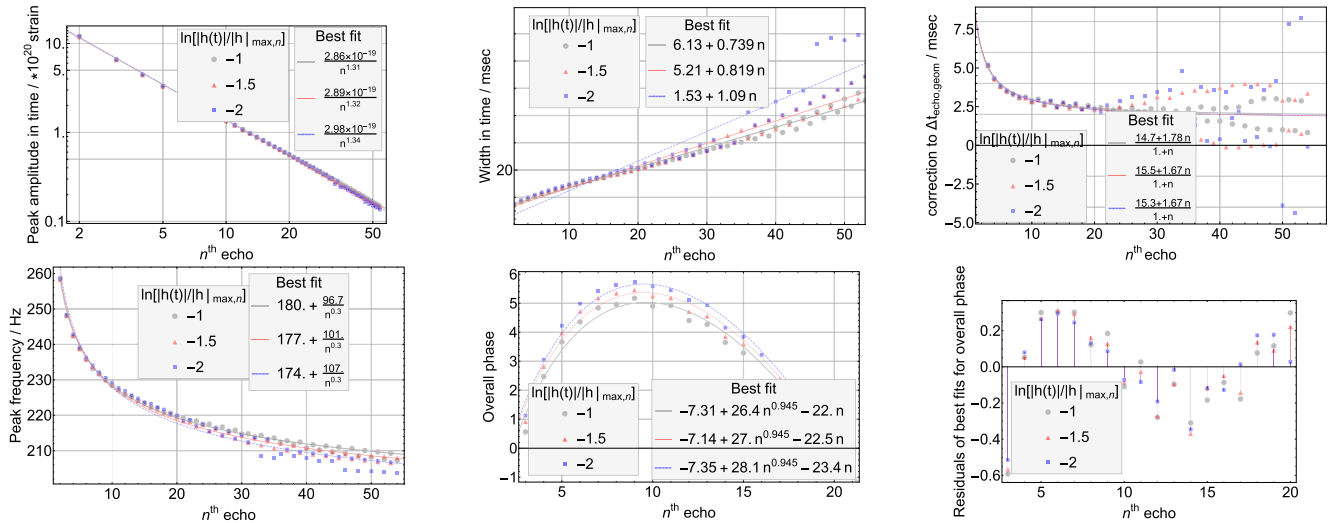

FIG. 7.   Best-fit Gaussian template parameters (for $\ln[|h(t)|/|h|_{\text{max,n}}] > -1, -1.5$ or -2), in our minimal model of LIGO event GW150914, showing second and later echoes. The top three panels are in the time domains. Starting from left, peak amplitudes of echoes in time are fit well by power laws. The middle panel is the width of the echoes, which become wider in time, as the high frequencies leak out more quickly. For the same reason, the peak frequency (bottom left) also decays with time. The top right panel gives corrections to $\Delta t_{\text{echo,geom}}$ [Eq. (15)]. Finally, the bottom middle and right provide the overall phase at t_{center} of each echo and the residuals of the best fit. This is the only plots in which we show the residuals since the numerical error for the phase is relatively big.
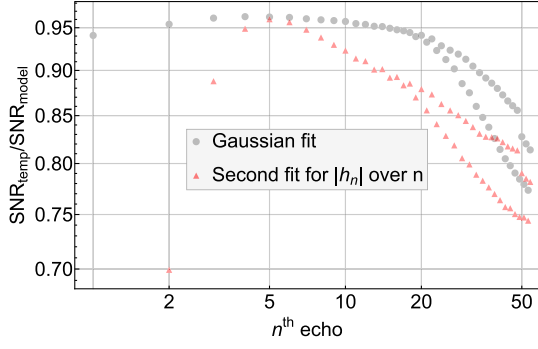
FIG. 8. SNR_{temp} compared to SNR_{model}, showing the quality of Gaussian templates.

delay, shown as Fig. 7, do not have a simple behavior. However, the power law fit to the peak amplitude in time $\propto n^{-4/3}$ is surprisingly good. Also, as we discussed before, since the shapes of the first few echoes are much more dependent on the initial conditions, it might be better to use independent Gaussians to fit them in data. Finding a reasonable fit for phase information Φ_n vs n proves even more challenging, as a small change in phase leads to a significant change in echo profiles. Fortunately,

model-agnostic searches (e.g., Ref. [35]) based on cross-correlating different detectors can be done independently of the phase information.

VI. BEYOND THE MINIMAL MODEL

While our minimal model for echoes has only one free parameter (the wall distance to the horizon, d_{wall}) in addition to those of GR, the reality can be more complicated. Here, we explore the two main deviations expected from the minimal model due to nonlinear effects in GR and quantum gravity.

A. Nonlinear mergers effects

Our assumption of a custom-designed incoming wave packet, as a placeholder for a black hole binary merger, is almost certainly too naive to provide a realistic echo template, as it misses the nonlinear nature of the merger. While numerical simulations can now provide realistic waveforms for black hole mergers in GR, a covariant formulation of ECOs that could produce realistic echo waveforms is currently missing. However, we can get an idea about the extent of nonlinear corrections to linear
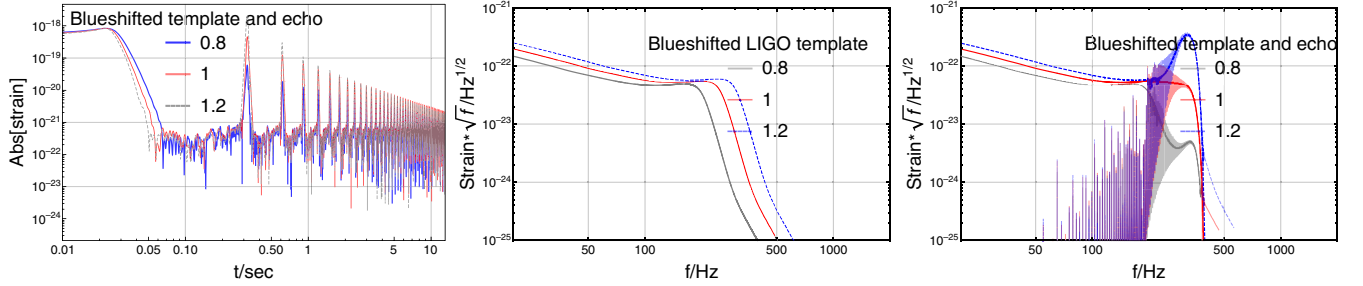

FIG. 9.   Echoes predicted for GW150914, expected for redshifted (blueshifted) initial conditions with respect to our minimal model. We see that lower frequency initial conditions lead to lower amplitude, but more persistent, echoes as they cannot penetrate the angular momentum barrier efficiently.
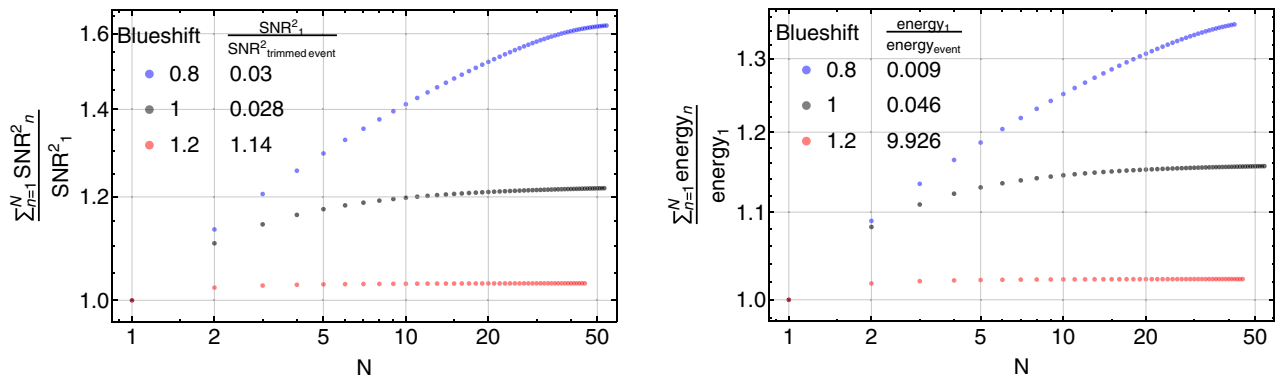

FIG. 10.   SNR and energy for blueshifted echoes compared with the first echo. We see that there is more (less) information in subsequent echoes for lower (higher) frequency initial conditions. Furthermore, the amplitude of the first echo is hard to predict and can change by more than 1.5 orders of magnitude. We also list SNRs and energy for blueshifted first echoes compared with the event. Since we assume white noise to calculate the SNR in time domain, we trim the merger template at around 0.076 sec before the peak (similar to the LIGO noise whitening for GW150914 template).

TABLE IV.   Same as Table III, but contrasting with redshifted/blueshifted initial conditions, fitted within $\ln\left[|h(t)|/|h|_{\mathrm{max,n}}\right] > -1.5$.

Blueshift factor s	0.8	1	1.2
Peak amplitude in time (strain)	$5.91 \times 10^{-20}/n^{1.14}$	$2.92 \times 10^{-19}/n^{1.33}$	$5.31 \times 10^{-19}/n^{1.54}$
Width in time (msec)	$3.91 + 0.678n$	$5.5 + 0.808n$	$9.48 + 0.711n$
Correction to $\Delta t_{\mathrm{echo,geom}}$ (msec)	$-47.8 - 57.0/(1+n)$	$15.4 + 1.64/(1+n)$	$76.2 + 60.4/(1+n)$
Peak frequency (Hz)	$227 + 95.2/n^{0.3}$	$175 + 104/n^{0.3}$	$144 + 97.8/n^{0.3}$
Overall phase	$-3.06 + 30.2n^{0.945} - 25.9n$	$-6.65 + 28.5n^{0.945} - 23.8n$	$-12.7 + 35.2n^{0.945} - 29.4n$

results by noticing that the Kerr background for the Teukolsky equation (1) is dynamical during the merger event, and thus the frequencies can be shifted by $\mathcal{O}(30\%)$, between the ingoing and outgoing waves at merger [58]. We shall explore the extent of this effect on echoes by introducing a blueshift parameter s, in the ingoing linear initial conditions:

$$\hat{h}_{\mathrm{LIGO,shifted}}[f] = \hat{h}_{\mathrm{LIGO}}[f/s]. \qquad (21)$$

As shown in Fig. 9, redshifted (blueshifted) initial conditions give echoes which damp more slowly (quickly), since low frequencies leak more slowly through the angular momentum barrier. This also dramatically changes the amplitude of the first few echoes. Blueshift parameter s can be a free parameters for data-fitting purposes.

The effect is clearer if we compare the SNR of echoes to the first echo, as shown in Fig. 10. SNR_n^2 is SNR^2 of our numerical solution of the nth echo, and we trimmed a single echo with $\ln\left[|h(t)|/|h|_{\mathrm{max,n}}\right] > -1.5$. We assume white Gaussian noise $\sigma_\omega = 1$ so that

$$\mathrm{SNR}_n^2 = \sum_\omega \frac{|\hat{h}_{n,\omega}|^2}{\sigma_\omega{}^2} = \sum_t |h_n|^2. \qquad (22)$$

Figure 10 (right panel) shows that later echoes contain more (less) information in redshifted (blueshifted)

templates, since they decay more slowly (quickly). The left panel also shows the relative SNR of the first echo compared to the trimmed main event in our model. The fact that this number can change by more than 1.5 orders of magnitude suggests that the amplitude of the first echo is very sensitive to the nonlinear merger physics and cannot be reliably predicted. Reference [59] simulates a binary black hole merger and finds the ratio of the energy falling into the black hole to the energy out is around 1:1, which can be used as a normalization of amplitude of echoes.

Table IV and Fig. 11 compare the best-fit echo parameters for different blueshift factors. We see in the left panels that the blueshifted initial condition ($s = 1.2$) has a transient excess in amplitude that decays quickly and falls in line with the minimal model. In contrast, the redshifted model ($s = 0.8$) has a significantly smaller but more persistent amplitude. Surprisingly, the middle panels show that the redshifted echoes remain narrower in time. Even more puzzling is that the redshifted initial conditions have higher frequency echoes as shown in Fig. 11's bottom left panel. This is due to the fact that the echo peak frequency depends on the slope (and not the amplitude) of the spectral density $\hat{h}_{\mathrm{out}}(\omega) = R_{\mathrm{ECO}}(\omega) \frac{\hat{h}_{\mathrm{LIGO}}(\omega)}{R_{\mathrm{BH}}(\omega)} f_{\mathrm{cutoff}}(\omega)$ from Eq. (11), which involves several complicated components. As we see in the middle panel of Fig. 9, this slope is not monotonic, which leads to the counterintuitive behavior, even though
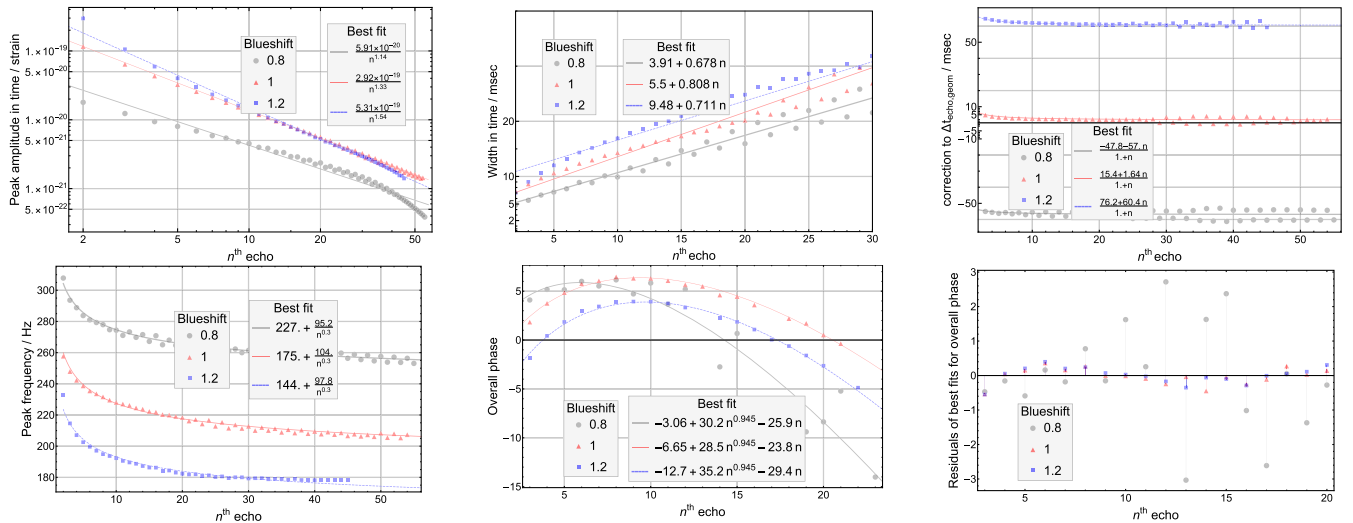

FIG. 11.   Same is Fig. 7, but using the different blueshift factors s [Eq. (21)] for echo initial conditions (fitted for $\ln\left[|h(t)|/|h|_{\mathrm{max,n}}\right] > -1.5$). We see that redshifted initial conditions yield weaker, but more persistent, echoes (see the text for details).
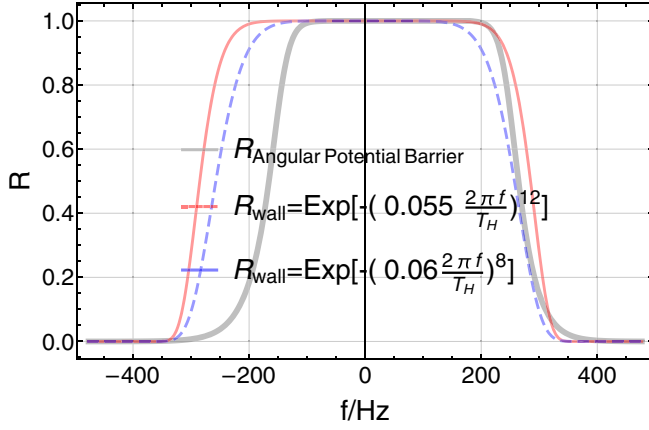
FIG. 12. Comparison of soft wall reflectivity coefficients that we use, with that of the Kerr angular momentum barrier [42]. The thin and dashed lines are the two reflectivity rates used in Fig. 13.
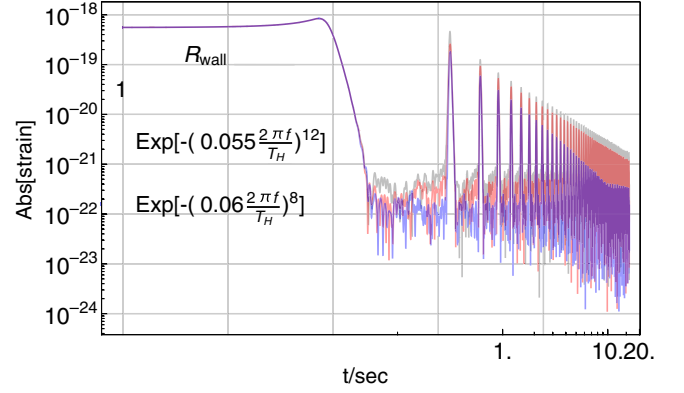

FIG. 13. Echoes for GW15014, for soft vs perfect walls. The top (gray) curve assumes a perfect wall/mirror, while the lower curves show soft walls with different energy reflectivity coefficients.

the amplitude of the redshifted model is smaller compared to the blueshifted one.

B. Soft wall

Motivated by quantum models of black holes, the wall must at least partially absorb the energy incident on the wall [31]. For example, in fuzzball models [6], high energy particles (with $\hbar\omega \gg kT_H$, where T_H is the Hawking temperature) excite the fuzzball microstates and thus will be absorbed by the wall. On the other hand, particles with $\hbar\omega \lesssim kT_H$ may be (at least partially) reflected (but see Ref. [60] for recent counterarguments). The ringdown phase of mergers of two BHs is in the intermediate range (~ 100 Hz for GW150914). Therefore, a realistic quantum gravity model for the echoes is expected to involve a *soft* wall. For example, the frequency of electromagnetic emissions from accretion into BHs is much higher, which is expected to be absorbed by the wall [61,62]. However, possible loopholes that could lead to astrophysical observables from quantum effects have been exploited in Refs. [15,63].

A wall that absorbs high frequency modes will dramatically decrease the amplitude of the first echo, since these modes leak out quickly every time the wave packet hits the angular momentum barrier. Therefore, the first echo contains most of the high frequency modes which, as shown in

the top left panel in Fig. 14, would be absorbed for a soft wall.

Of course, the actual frequency-dependent reflection of the wall depends on the specific quantum theory of black holes. We explore a phenomenological model for the wall with a Gaussian-like energy reflection rate,

$$R_{\text{wall}}(\omega) \simeq \exp\left[-\left(\alpha\frac{\omega}{T_H}\right)^q\right], \qquad (23)$$

where $T_H = \frac{r_+^2 - a^2}{4\pi r_+(r_+^2 + a^2)}$ is the Hawking temperature for Kerr BH. While smooth R_{wall}'s, such as Gaussian or Boltzmann reflectivity ($q = 2$ or 1, respectively) may appear natural, they do tend to essentially wipe out the echoes, unless $\alpha \ll 1$, which is inconsistent with the tentative echoes found in Ref. [31]. In contrast, a sharper function with, e.g., $q = 12$ then can damp the first echo, but not significantly influence later echoes, as shown in Fig. 13 [64]. We can also compare these reflectivity functions with that of the angular momentum barrier of the Kerr BH, for the same spin and mass, as shown in Fig. 12, which provides another motivation for sharper R_{wall}'s.

Table V and Fig. 14 compare the template for the perfect and soft walls, similar to Figs. 7 and 11. We see in the top left panel that, due to absorption of high frequency modes,

TABLE V. Same as Table III, but contrasting perfect ($R_{\text{wall}} = 1$) and soft ($R_{\text{wall}} = \exp[-(0.055\frac{\omega}{T_H})^{12}]$) walls, fitted within $\ln[|h(t)|/|h|_{\text{max,n}}] > -1.5$.

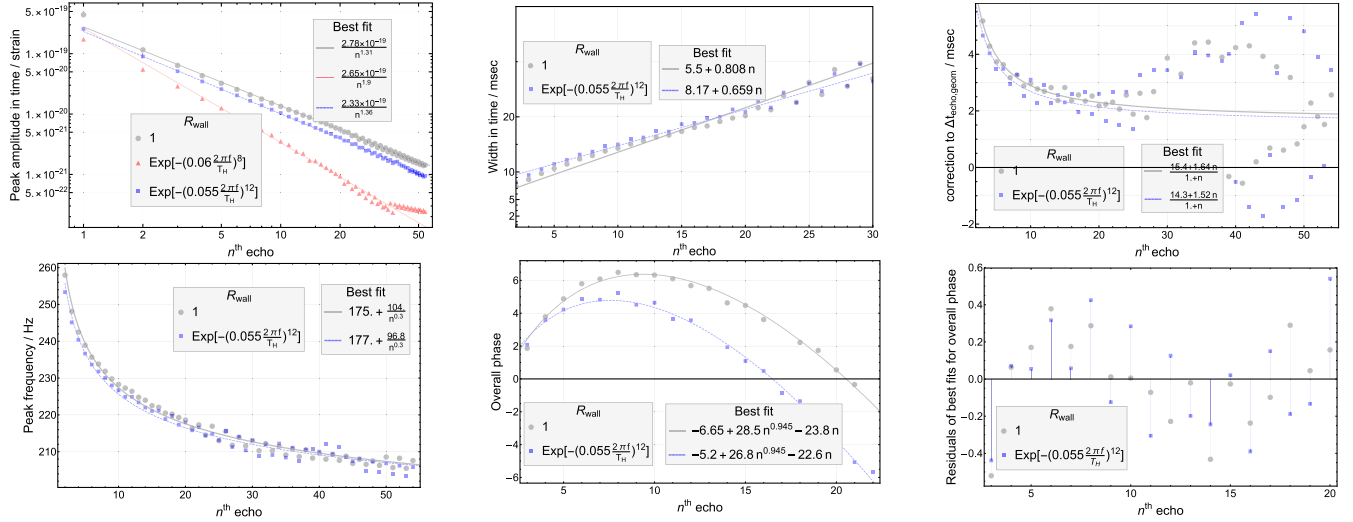| Wall type	Perfect	Soft
Peak amplitude in time (strain)	$2.78 \times 10^{-19}/n^{1.31}$	$2.33 \times 10^{-19}/n^{1.36}$
Width in time (msec)	$5.5 + 0.808n$	$8.17 + 0.659n$
Correction to $\Delta t_{\text{echo,geom}}$ (msec)	$15.4 + 1.64/(1 + n)$	$14.3 + 1.52/(1 + n)$
Peak frequency (Hz)	$175 + 104/n^{0.3}$	$177 + 96.8/n^{0.3}$
Overall phase	$-6.65 + 28.5n^{0.945} - 23.8n$	$-5.2 + 26.8n^{0.945} - 22.6n$

FIG. 14. Same as Fig. 7, comparing walls with different energy reflectivity coefficients (fitted for $\ln[|h(t)|/|h|_{\max,n}] > -1.5$). We see that echo amplitudes and peak frequencies decay more quickly for softer walls (see the text for details).

the power law fit to the amplitudes could be extended to the first echo for the soft walls. More generally, echoes decay faster for a softer wall. As echoes for a wall with $R_{\text{wall}} = \exp[-(0.06 \frac{\omega}{T_H})^8]$ decay too fast, we only focus on the $R_{\text{wall}} = \exp[-(0.055 \frac{\omega}{T_H})^{12}]$ case in subsequent panels of Fig. 14 and provide numerical fits for echo properties in Table V. With this choice, the evolution of echo properties is similar to those in Figs. 7 and 11, with the notable difference that peak frequency decays more rapidly as the soft wall absorbs high frequencies.

VII. CONCLUSIONS

We have provided realistic templates for echoes of BH mergers by numerically solving the linearized Einstein equation (or Teukolsky equation) in Kerr spacetime with boundary conditions at a Planck length proper distance outside the (would-be) event horizon. We obtain analytic approximations for the echo waveforms and time delays and explore their dependence on the softness of the wall (or frequency dependence of the reflection rate), as well as nonlinear effects during the merger event. These analytic templates should be useful in echo searches in current and future gravitational wave data. Finally, we studied the occurrence of superradiant instability and showed that it has a negligible effect, for the first few dozen echoes of in typical BH mergers such as GW150914.

Let us close with some open questions and future directions:

(i) The strain is dominated by mode $l = 2$, $m = \pm 2$. We only show mode $m = 2$ here, and the solution of $m = -2$ can easily be found by $R_{slm}[\omega] = R^*_{sl-m}[-\omega]$. More realistic templates should combine all other modes by the appropriate weight.

(ii) We cannot provide a reliable waveform for the first echo as it is too sensitive to the *ad hoc* cutoff function (13) that we use to set up our initial conditions. This highlights the need for a covariant numerical implementation of ECOs within a dynamical spacetime, which could provide realistic nonlinear initial conditions for echoes.

(iii) Another big uncertainty is the expected softness of the wall. While this is ultimately a question for the quantum models of black holes, it highlights the need for a covariant and causal description of the wall dynamics. It might be possible to describe this dynamics in terms of the properties of a surface (2+1d) fluid and Israel junction conditions (e.g., see Ref. [16]).

(iv) The computation of the echo phase beyond ∼20 echoes is limited by numerical precision and frequency resolution. This can be improved in the future, by either brute force or novel numerical/ analytic methods.
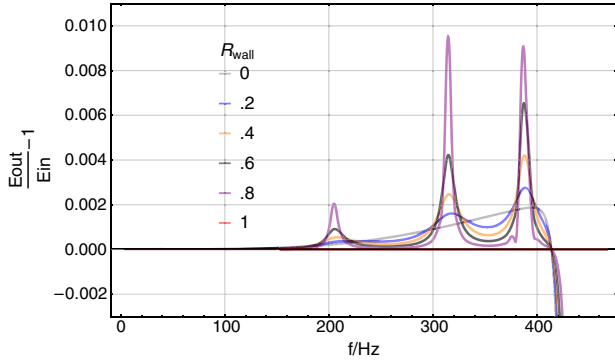
FIG. 15. Superradiance by a spinning ECO/BH with $a = 0.99$ and $M = 67.6 M_\odot$, assuming different wall reflection coefficients R_{wall}^{1}, with wall position $r_{\text{wall}} = r_{\text{h}}(1 + \delta), \delta = 0.05$. The horizontal axis is the frequency, while the vertical axis is the relative energy extracted from the ECO/BH. $R_{\text{wall}} = 0$ is the classical BH (with no reflection on the horizon), showing a smooth response with superradiance at low frequencies. A soft wall with $0 < R_{\text{wall}} < 1$ shows several peaks, corresponding to the resonance frequencies of the cavity formed by the wall and the angular momentum barrier, which amplify superradiance. A perfect reflective wall kills superradiance by definition, as all the energy that goes in comes out eventually.

APPENDIX: ERGOREGION INSTABILITY

In this Appendix, we further discuss the emergence of superradiance and ergoregion instability in ECOs.

Figure 15 shows the superradiance in the frequency domain. We notice that the amplification develops resonance peaks in the presence of an imperfect wall [66], and these peaks become sharper with increasing the reflectivity of the wall. However, a perfect wall seems to kill the superradiance for scattered waves. It is much more plausible that we in fact develop infinitely sharp resonance peaks, associated with trapped ergoregion w-modes, which cannot be captured by finite resolution in the frequency domain. We integrate the plots over the superradiance range for different reflectivity of the wall, shown in Table VI. The area is roughly conserved for all soft walls and equal to the area of a classical BH. Hence, we conclude that when approaching $R_{\text{wall}} = 1$ we still have the superradiance, but only at discrete frequencies. The zeros of both Fig. 15 and Table VI are just because of finite resolution in the frequency domain, and we are not able to see the infinitely sharp resonances when approaching $R_{\text{wall}} \to 1$.

Figure 16 shows that resonance superradiant peaks disappear as $a \to 0$, while Fig. 17 shows that they shift when we shift the position of the wall, as expected.

Note that, even in the absence of superradiant scattering, there could still be instabilities that manifest

TABLE VI. Integrals of superradince profiles (curves in Fig. 15, up to the superradiance threshold) for different wall positions δ, or absorptions R_{wall}. We see that the integrated superradiance appears to have a universal value, independent of the wall presence or properties. The same is likely to be the case of the perfect wall (last row) but cannot be resolved numerically due to infinitely sharp resonance structure.

$\delta =$	0.05	0.015	0.0005
$R_{\text{wall}} = 0$	0.2202	0.2202	0.2202
0.2	0.2226	0.2226	0.2225
0.4	0.2246	0.2246	0.2243
0.6	0.2260	0.226r	0.2256
0.8	0.2223	0.2276	0.2190
1	0.0000	0.0000	0.0000

themselves as the poles of the amplification in the upper complex plane of frequency space. Indeed, ergoregion instability was predicted in Ref. [44] in the absence of horizons and/or dissipation. However, we do not see any significant growth, at least in the first 50 echoes we predict for GW150914 in Fig. 3. This can be understood by noticing that, as shown in Fig. 7, the echoes are dominated by frequencies $f \gtrsim 210$ Hz, but superradiance happens at $f < m\Omega_H \simeq 180$ Hz for this event. Hence, the instability does not take over until peak frequency drops below this limit.

We can increase the spin to see the superradiant instability develop faster, as shown in Fig. 18. For spin $a = 0.80$, the echoes stop decaying at some point, and for $a = 0.99$, they start to increase. While this example does demonstrate the appearance of ergoregion instability, it should be treated as a toy model, as the initial wave packet was designed to reproduce the merger/ringdown template LIGO event GW150914 with $a = 0.67$.

As we mentioned in Sec. I, whether or not ergoregion instability acts in nature depends on the wall absorption properties [49]. Indeed, observation of astrophysical black holes at significant spins [48] does suggest that the instability must be suppressed.
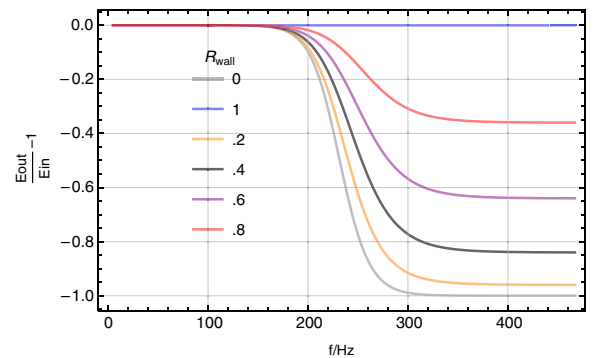

FIG. 16. Same as Fig. 15, but with $a = 0$. We see that superradiance and superradiant resonance peaks disappear as spin goes to zero.

---

[1]For simplicity, we present results with scalar mode $(l, m, s) = (2, 2, 0)$, but we have confirmed the same results for gravitational waves.
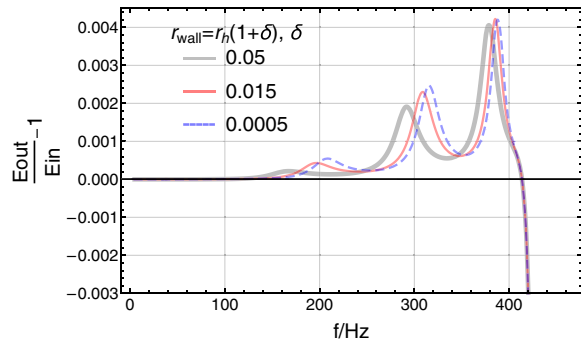
FIG. 17. Same as Fig. 15, but with different wall positions (fixing $R_{wall} = 0.4$). We see that this shifts the resonance frequencies.
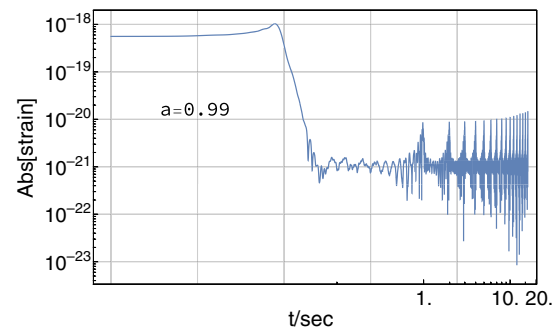

FIG. 18. Occurrence of ergoregion instability in later echoes in ECOs with higher spin (near extremal Kerr).

[1] P. O. Mazur and E. Mottola, Proc. Natl. Acad. Sci. U.S.A. **101,** 9545 (2004).

[2] O. Lunin and S. D. Mathur, Nucl. Phys. **B623,** 342 (2002).

[3] O. Lunin and S. D. Mathur, Phys. Rev. Lett. **88,** 211303 (2002).

[4] S. D. Mathur, Fortsch. Phys. **53,** 793 (2005).

[5] S. D. Mathur, arXiv:0810.4525

[6] S. D. Mathur and D. Turton, J. High Energy Phys. 01 (2014) 034.

[7] S. L. Braunstein, S. Pirandola, and K. Życzkowski, Phys. Rev. Lett. **110,** 101301 (2013).

[8] A. Almheiri, D. Marolf, J. Polchinski, and J. Sully, J. High Energy Phys. 02 (2013) 062.

[9] C. Barcel, R. Carballo-Rubio, and L. J. Garay, Universe **2,** 7 (2016).

[10] H. Kawai and Y. Yokokura, Universe **3,** 51 (2017).

[11] P. Hayden and J. Preskill, J. High Energy Phys. 09 (2007) 120.

[12] Y. Sekino and L. Susskind, J. High Energy Phys. 10 (2008) 065.

[13] N. Afshordi, arXiv:0807.2639.

[14] C. Prescod-Weinstein, N. Afshordi, M. L. Balogh, N. Afshordi, and M. L. Balogh, Phys. Rev. D **80,** 043513 (2009).

[15] N. Afshordi and Y. K. Yazdi, Classical Quantum Gravity **33,** 235017 (2016).

[16] M. Saravani, N. Afshordi, and R. B. Mann, Int. J. Mod. Phys. D **23,** 1443007 (2014).

[17] B. Holdom and J. Ren, Phys. Rev. D **95,** 084034 (2017).

[18] B. P. Abbott et al. (Virgo and LIGO Scientific Collaborations), Phys. Rev. Lett. **116,** 131103 (2016).

[19] B. P. Abbott et al. (Virgo and LIGO Scientific Collaborations), Phys. Rev. X **6,** 041015 (2016).

[20] S. B. Giddings, Classical Quantum Gravity **33,** 235010 (2016).

[21] B. P. Abbott et al. (Virgo and LIGO Scientific Collaborations), Phys. Rev. Lett. **116,** 061102 (2016).

[22] B. P. Abbott et al. (Virgo and LIGO Scientific Collaborations), Phys. Rev. Lett. **116,** 241103 (2016).

[23] B. P. Abbott et al. (VIRGO and LIGO Scientific Collaborations), Phys. Rev. Lett. **118,** 221101 (2017).

[24] B. P. Abbott et al. (Virgo and LIGO Scientific Collaborations), Phys. Rev. Lett. **119,** 141101 (2017).

[25] B. Abbott et al. (Virgo and LIGO Scientific Collaborations), Phys. Rev. Lett. **119,** 161101 (2017).

[26] B. P. Abbott et al. (Virgo and LIGO Scientific Collaborations), Astrophys. J. **851,** L35 (2017).

[27] V. Cardoso, E. Franzin, and P. Pani, Phys. Rev. Lett. **116,** 171101 (2016); **117,** 089902(E) (2016).

[28] V. Cardoso, S. Hopper, C. F. B. Macedo, C. Palenzuela, and P. Pani, Phys. Rev. D **94,** 084031 (2016).

[29] V. Cardoso and P. Pani, arXiv:1707.03021.

[30] V. Cardoso and P. Pani, Nat. Astron. **1,** 586 (2017).

[31] J. Abedi, H. Dykaar, and N. Afshordi, Phys. Rev. D **96,** 082004 (2017).

[32] G. Ashton, O. Birnholtz, M. Cabero, C. Capano, T. Dent, B. Krishnan, G. D. Meadors, A. B. Nielsen, A. Nitz, and J. Westerweck, arXiv:1612.05625.

[33] J. Westerweck, A. Nielsen, O. Fischer-Birnholtz, M. Cabero, C. Capano, T. Dent, B. Krishnan, G. Meadors, and A. H. Nitz, arXiv:1712.09966.

[34] J. Abedi, H. Dykaar, and N. Afshordi, arXiv:1701.03485.

[35] R. S. Conklin, B. Holdom, and J. Ren, arXiv:1712.06517.

[36] J. Abedi and N. Afshordi, arXiv:1803.10454.

[37] A. Maselli, S. H. Vlkel, and K. D. Kokkotas, Phys. Rev. D **96,** 064045 (2017).

[38] R. H. Price and G. Khanna, Classical Quantum Gravity **34,** 225005 (2017).

[39] Z. Mark, A. Zimmerman, S. M. Du, and Y. Chen, Phys. Rev. D **96,** 084002 (2017).

[40] S. H. Vlkel and K. D. Kokkotas, Classical Quantum Gravity **35,** 105018 (2018).

[41] S. H. Vlkel and K. D. Kokkotas, Classical Quantum Gravity **34,** 175015 (2017).

[42] H. Nakano, N. Sago, H. Tagoshi, and T. Tanaka, Prog. Theor. Exp. Phys. (**2017**) 071E01.

[43] P. Bueno, P. A. Cano, F. Goelen, T. Hertog, and B. Vercnocke, Phys. Rev. D **97**, 024040 (2018).

[44] J. L. Friedman, Commun. Math. Phys. **63**, 243 (1978).

[45] V. Cardoso, P. Pani, M. Cadoni, and M. Cavaglia, Phys. Rev. D **77**, 124044 (2008).

[46] P. V. P. Cunha, E. Berti, and C. A. R. Herdeiro, Phys. Rev. Lett. **119**, 251102 (2017).

[47] S. Hod, Phys. Lett. B **736**, 398 (2014).

[48] R. Narayan and J. E. McClintock, arXiv:1312.6698.

[49] E. Maggio, P. Pani, and V. Ferrari, Phys. Rev. D **96**, 104047 (2017).

[50] However, we should note that the echoes reported in Refs. [31,35] are for different events, even though they are both broadly consistent with the hypothesis of near-horizon Planck-scale structure.

[51] S. A. Teukolsky, Astrophys. J. **185**, 635 (1973).

[52] E. Berti, V. Cardoso, and M. Casals, Phys. Rev. D **73**, 024013 (2006); **73**, 109902(E) (2006).

[53] R. Brito, V. Cardoso, and P. Pani, Lect. Notes Phys. **906**, 1 (2015).

[54] https://losc.ligo.org/events/GW150914/.

[55] https://centra.tecnico.ulisboa.pt/network/grit/files/amplification-factors/.

[56] W. H. Press and S. A. Teukolsky, Nature (London) **238**, 211 (1972).

[57] M. R. Correia and V. Cardoso, Phys. Rev. D **97**, 084030 (2018).

[58] Given the symmetries of Eqs. (3) and (4), we can easily extend the solution to the $m = -2$ case using $R_{slm}[\omega] = R^*_{sl-m}[-\omega]$.

[59] A. Gupta, B. Krishnan, A. Nielsen, and E. Schnetter, Phys. Rev. D **97**, 084028 (2018).

[60] B. Guo, S. Hampton, and S. D. Mathur, arXiv:1711.01617.

[61] A. E. Broderick, A. Loeb, and R. Narayan, Astrophys. J. **701**, 1357 (2009).

[62] A. E. Broderick, R. Narayan, J. Kormendy, E. S. Perlman, M. J. Rieke, and S. S. Doeleman, Astrophys. J. **805**, 179 (2015).

[63] U.-L. Pen and A. E. Broderick, Mon. Not. R. Astron. Soc. **445**, 3370 (2014).

[64] For example, the best fit for the dominant quasinormal mode frequency for GW150914 is 10%–20% offset from the linear theory predictions for the best-fit Kerr metric (Fig. 5 in Ref. [65]).

[65] B. P. Abbott et al. (Virgo and LIGO Scientific Collaborations), Phys. Rev. Lett. **116**, 221101 (2016).

[66] Figure 13 also shows that if the wall absorbs too much the late echoes will stop decaying. This is due to superradiant instability which we shall discuss in the next section.

[67] W. G. Unruh and R. M. Wald, Rep. Prog. Phys. **80**, 092002 (2017).